

# High-efficiency small-molecule ternary solar cells with a hierarchical morphology enabled by synergizing fullerene and non-fullerene acceptors

Zichun Zhou<sup>1,2,5</sup>, Shengjie Xu<sup>1,5</sup>, Jingnan Song<sup>3</sup>, Yingzhi Jin<sup>4</sup>, Qihui Yue<sup>1,2</sup>, Yuhao Qian<sup>3</sup>, Feng Liu<sup>3\*</sup>, Fengling Zhang<sup>4\*</sup> and Xiaozhang Zhu<sup>1,2\*</sup>

**Using combinatory photoactive blends is a promising approach to achieve high power conversion efficiency in ternary organic photovoltaics. However, the fundamental challenge of how to manipulate the morphology of multiple components and correlate structure details via device performance has not been well addressed. Achieving an ideal morphology that simultaneously enhances charge generation and transport and reduces voltage loss is an imperative avenue to improve device efficiency. Here, we achieve a high power conversion efficiency of  $13.20 \pm 0.25\%$  for ternary solar cells by using a combination of small molecules with both fullerene and non-fullerene acceptors, which form a hierarchical morphology consisting of a PCBM transporting highway and an intricate non-fullerene phase-separated pathway network. Carrier generation and transport find an optimized balance, and voltage loss is simultaneously reduced. Such a morphology fully utilizes the individual advantages of both fullerene and non-fullerene acceptors, demonstrating their indispensability in organic photovoltaics.**

Employing multiple light-absorbing materials to broaden the absorption spectrum has been recognized as an efficient approach to realize high power conversion efficiency (PCE) in ternary organic photovoltaics (TOPVs)<sup>1–3</sup>. TOPV performance strongly relies on materials combinations that can form matched electronic structure and proper blend morphology for charge generation and transport. In spite of a few recent successful examples<sup>4–10</sup>, the fundamental challenge of how to manipulate the morphology of multi-component blends, guided by balancing complicated dynamics and kinetics, to meet the need of extracting the maximum photon current and voltage and reduce the loss channels of different origins is far from being fulfilled. Achieving an ideal morphology that can maximize charge generation and extraction using suitable materials and treatments is an inevitable avenue for improving device efficiency. To this end, combining fullerene and non-fullerene acceptors (NFAs) can be advantageous as phenyl- $C_{61}$ -butyric acid methyl ester (PCBM) derivatives<sup>11,12</sup> are good electron transport media, while NFAs<sup>13–15</sup> have good light absorption and highly tunable energy-level alignment. In addition, energy losses<sup>16–19</sup> (defined as  $E_{\text{loss}} = E_{\text{g}}^{\text{opt}} - qV_{\text{oc}}$  (where  $E_{\text{g}}^{\text{opt}}$  is the optical bandgap,  $V_{\text{oc}}$  is the open-circuit voltage and  $q$  is elementary charge) are low in non-fullerene organic photovoltaics (OPVs) due to a small driving force during charge separation<sup>20</sup>. We are particularly interested in small-molecule OPVs<sup>21–24</sup> due to their mature synthesis and purification<sup>25</sup>. We have recently developed a series of low-bandgap NFAs<sup>26–28</sup> that can extend light absorption to the near-infrared (NIR) region based on the quinoid-resonance effect of thieno[3,4-*b*]thiophene<sup>29,30</sup>. To match with low-bandgap NFAs, high-bandgap molecular donors are targeted. A finite phase-separated morphology between donor and NFA can be used to secure large current generation; modified C70

fullerene (PC<sub>71</sub>BM) is introduced as a phase mediator and transport channel to guarantee good electron transport. Under this prescribed morphology, elevated device performance can be expected.

Here we use a high-bandgap and high-crystallinity molecular donor (BTR, benzodithiophene terthiophene rhodanine)<sup>31</sup>, a low-bandgap and moderate-crystallinity molecular acceptor (NITI)<sup>28</sup> and PC<sub>71</sub>BM to form a favourable cascade-energy-level alignment to develop high-performance ternary solar cells. A hierarchical morphology composed of PC<sub>71</sub>BM transporting highways and intricate non-fullerene phase-separated small pathways is obtained, where carrier generation and transport achieve an optimal balance. Such a morphology fully utilizes the individual advantages of both non-fullerene and fullerene acceptors, which demonstrates their necessity in OPVs. A  $V_{\text{oc}}$  of  $0.94 \pm 0.01$  V, short-circuit current ( $J_{\text{sc}}$ ) of  $19.53 \pm 0.38$  mA cm<sup>-2</sup>, fill factor (FF) of  $71.96 \pm 0.99\%$  and PCE of  $13.20 \pm 0.25\%$  counted from 35 devices are obtained at a substantial blend thickness of 300 nm. Balanced charge transport, efficient charge extraction, reduced bimolecular recombination and low  $E_{\text{loss}}$  (0.55 eV) are also recorded.

## Performance enhancement in ternary solar cells

Figure 1a,b shows the chemical structure and energy levels of the materials used in the ternary blends. The BTR:NITI and BTR:PC<sub>71</sub>BM energy levels are well aligned to split photon-generated excitons. PC<sub>71</sub>BM has deeper highest occupied molecular orbital and lowest unoccupied molecular orbital energy levels; thus, it can serve as an electron sink to host electrons and form electron transport channels. The absorption of these molecules is well complemented to cover the whole visible to NIR region (300–850 nm, Fig. 1c), from which a broad external quantum efficiency

<sup>1</sup>Beijing National Laboratory for Molecular Sciences, CAS Key Laboratory of Organic Solids, Institute of Chemistry, Chinese Academy of Sciences, Beijing, China. <sup>2</sup>School of Chemical Sciences, University of Chinese Academy of Sciences, Beijing, China. <sup>3</sup>Department of Physics and Astronomy and Collaborative Innovation Center of IFSA (CICIFSA), Shanghai Jiao Tong University, Shanghai, China. <sup>4</sup>Department of Physics, Chemistry and Biology (IFM), Linköping University, Linköping, Sweden. <sup>5</sup>These authors contributed equally: Zichun Zhou, Shengjie Xu. \*e-mail: [fengliu82@sjtu.edu.cn](mailto:fengliu82@sjtu.edu.cn); [fengling.zhang@liu.se](mailto:fengling.zhang@liu.se); [xzzhu@iccas.ac.cn](mailto:xzzhu@iccas.ac.cn)

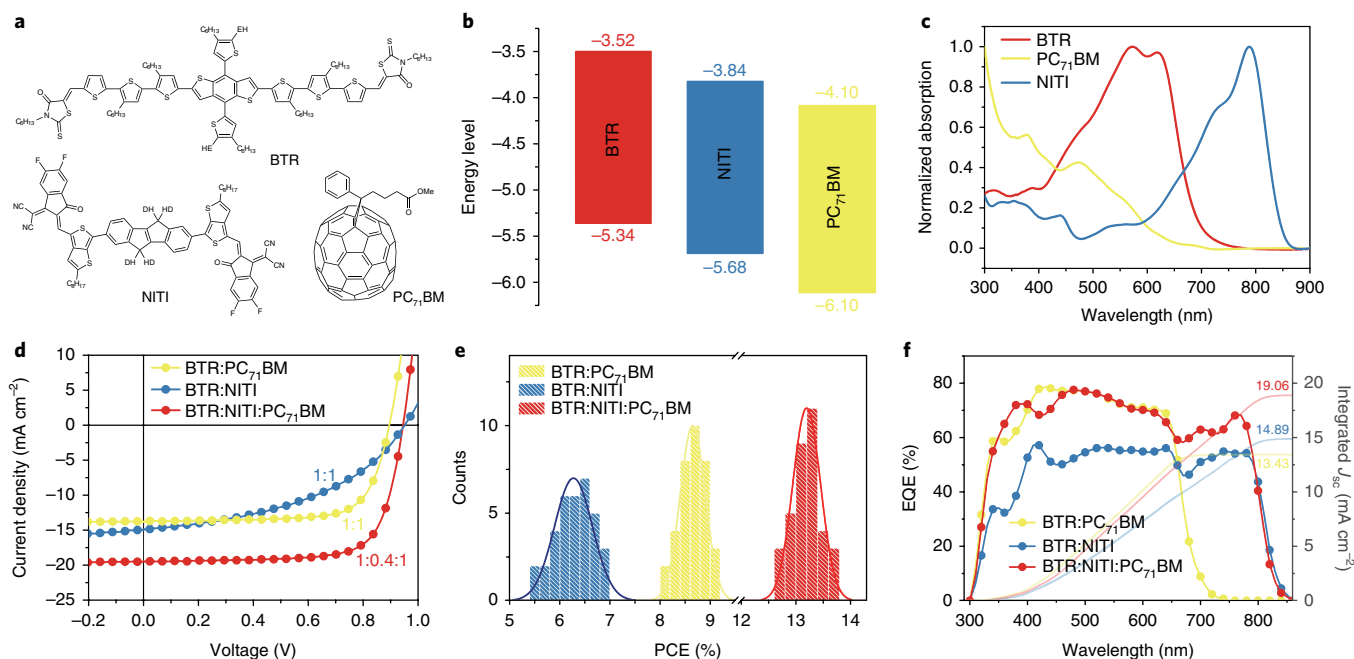


**Fig. 1 | Properties and photovoltaic performance.** **a**, Chemical structures of BTR, NITI and PC<sub>71</sub>BM in the ternary device. **b**, Energy levels of BTR, NITI and PC<sub>71</sub>BM. **c**, Normalized thin-film absorptions of BTR, NITI and PC<sub>71</sub>BM. **d**, Current-voltage characteristics of the binary and ternary devices under constant incident light intensity (AM 1.5G, 100 mW cm<sup>-2</sup>). **e**, Histogram of the PCE measurements for 35 devices based on binary- and ternary-blend films. The average PCE of BTR:NITI:PC<sub>71</sub>BM TOPVs is 13.20% with a standard deviation of 0.25 summarized from 35 devices. **f**, EQE and integrated  $J_{sc}$  of the binary and ternary devices.

**Table 1 | Summary of photovoltaic parameters in binary and ternary solar cells**

| BTR:NITI:PC <sub>71</sub> BM | Thickness (nm) | $V_{oc}$ (V)      | $J_{sc}$ (mA cm <sup>-2</sup> ) | Fill factor (%)     | PCE (%)             | $\mu_h$ (cm <sup>2</sup> V <sup>-1</sup> s <sup>-1</sup> ) | $\mu_e$ (cm <sup>2</sup> V <sup>-1</sup> s <sup>-1</sup> ) |
|------------------------------|----------------|-------------------|---------------------------------|---------------------|---------------------|--|--|
| 1:0:1                        | 250            | 0.90(0.89 ± 0.01) | 13.80(13.42 ± 0.41)             | 72.86(71.67 ± 0.90) | 9.03(8.66 ± 0.26)   | (4.43 ± 0.73) × 10 <sup>-4</sup>                           | (9.08 ± 0.22) × 10 <sup>-4</sup>                           |
| 1:1:0                        | 250            | 0.95(0.95 ± 0.01) | 15.02(14.33 ± 0.60)             | 48.69(46.99 ± 2.98) | 6.82(6.28 ± 0.39)   | (2.91 ± 0.25) × 10 <sup>-4</sup>                           | (1.27 ± 0.14) × 10 <sup>-5</sup>                           |
| 1:0.4:1                      | 300            | 0.94(0.94 ± 0.01) | 19.50(19.53 ± 0.38)             | 73.83(71.96 ± 0.99) | 13.63(13.20 ± 0.25) | (6.14 ± 0.65) × 10 <sup>-4</sup>                           | (5.50 ± 0.60) × 10 <sup>-4</sup>                           |

The average PCE values with standard deviations were obtained from 35 devices.

(EQE) response is expected. Binary (BOPVs) and ternary solar cells are fabricated using a conventional device structure and the post-treatment of tetrahydrofuran (THF) vapour annealing during morphology optimization, and detailed performance data are summarized in Fig. 1d and Table 1. The appropriate annealing time is critical in driving high device performance, with 60 s as the best condition in our experiment (Supplementary Table 1). The BTR:PC<sub>71</sub>BM blend shows a moderate efficiency of 8.66 ± 0.26%, and such a PC<sub>71</sub>BM-based blend suffers from a high  $E_{loss}$  of 0.92 eV. A good phase separation is expected due to the high-crystallinity nature of BTR and strong material demixing, which induces balanced transport channels and boosts the FF (71.67 ± 0.90%). Poor absorption from PC<sub>71</sub>BM leads to a low  $J_{sc}$  of 13.42 ± 0.41 mA cm<sup>-2</sup>. The BTR:NITI blend shows a low  $E_{loss}$  of 0.54 eV; thus, a high  $V_{oc}$  of 0.95 ± 0.01 V is obtained, which is quite important in non-fullerene OPVs<sup>32</sup>. Poor morphology caused by good material mixing in non-fullerene blends leads to a strong charge recombination; thus, a poor FF (46.99 ± 2.98%) is observed. The BTR:NITI:PC<sub>71</sub>BM (1:0.4:1) ternary blend combines the advantages of both fullerene and non-fullerene acceptors, whose devices treated by solvent vapour annealing (SVA) show a  $V_{oc}$  of 0.94 ± 0.01 V,  $J_{sc}$  of 19.53 ± 0.38 mA cm<sup>-2</sup>, FF of 71.96 ± 0.99% and PCE of 13.20 ± 0.25%. The good transport property of PC<sub>71</sub>BM and the low  $E_{loss}$  of the NFA are maintained, which increases the FF and  $V_{oc}$ . Though PC<sub>71</sub>BM has poor absorption, its presence improves the EQE response in the BTR:NITI blend

to a high level, especially in the NIR region (Fig. 1f), indicating that PC<sub>71</sub>BM-dominated electron transport is critical and benefits both the BTR and NITI domains. Ternary blends of different compositions were investigated and mostly displayed improvements in the device parameters (Supplementary Tables 2 and 3). Maintaining a high PC<sub>71</sub>BM content is critical for obtaining a high PCE, as it indicates the importance of PC<sub>71</sub>BM moiety during morphology optimization. The consistency in device performance indicates that our new ternary methodology has high composition tolerance, which should be lied in a new morphology that can maximize the advantages of a non-fullerene electronic process and PC<sub>71</sub>BM transport. Single carrier devices were fabricated to evaluate electron and hole mobilities using the space charge limited current (SCLC) model (Supplementary Table 4). The BTR:PC<sub>71</sub>BM binary blend shows good hole ( $\mu_h$ ) and electron ( $\mu_e$ ) mobilities of (4.43 ± 0.73) × 10<sup>-4</sup> and (9.08 ± 0.22) × 10<sup>-4</sup> cm<sup>2</sup> V<sup>-1</sup> s<sup>-1</sup>, respectively, due to well-defined phase separation and BTR crystallization. The BTR:NITI binary blend shows a moderate  $\mu_h$  of (2.91 ± 0.25) × 10<sup>-4</sup> cm<sup>2</sup> V<sup>-1</sup> s<sup>-1</sup> and quite low  $\mu_e$  of (1.27 ± 0.14) × 10<sup>-5</sup> cm<sup>2</sup> V<sup>-1</sup> s<sup>-1</sup> due to excessive material mixing and low NITI crystallinity. The ternary bulk-heterojunction (BHJ) blend shows balanced hole and electron mobilities of (6.14 ± 0.65) × 10<sup>-4</sup> and (5.50 ± 0.60) × 10<sup>-4</sup> cm<sup>2</sup> V<sup>-1</sup> s<sup>-1</sup>, respectively, within a high-value range, which explains the improved FF of the device. The ternary blend shows enhanced device performance at varied thicknesses, with an optimal performance at 300 nm and

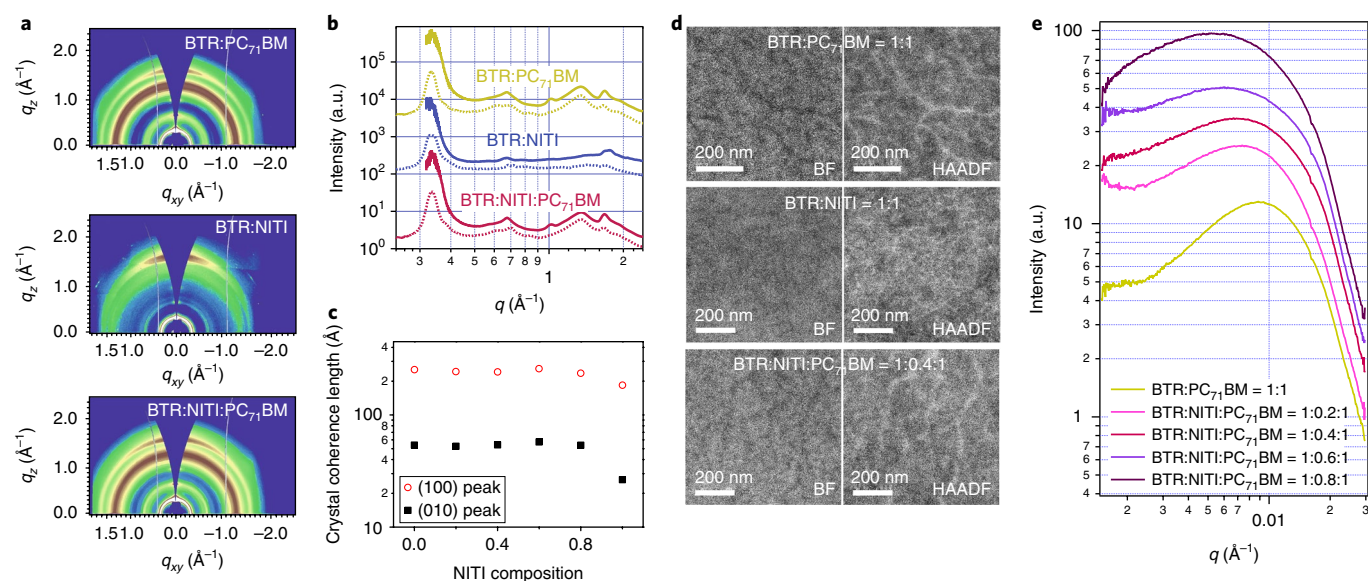


**Fig. 2 | Morphology investigations.** **a**, GIWAXS two-dimensional diffraction patterns of the binary and ternary blends (1:0.4:1). **b**, In-plane (dotted lines) and out-of-plane (solid lines) line-cut profiles of the two-dimensional GIWAXS data. **c**, Length information of the crystallinity coherence for the blended films with different NITI compositions. **d**, Bright-field (BF, left column) and HAADF (right column) TEM of the binary and ternary blends. **e**, RSoXS scattering profiles of the binary and ternary BHJ thin films using a photon energy of 284.2 eV.  $q$ , scattering vector.

a high average PCE of  $10.56 \pm 0.23\%$  maintained at a 500 nm thickness (Supplementary Table 5). It is quite rare to obtain high-performance small-molecule OPVs with a large thickness due to limited transport ability<sup>31,33</sup>. Thus, our system reveals a device functioning mechanism that can surpass this limitation. We obtained consistently high PCEs for a wide variety of devices, with an average PCE of 13.20% (Fig. 1e). The ternary solar cells were encapsulated and certified by the National Institute of Metrology in China, showing a 12.9% PCE (Supplementary Fig. 20), which is the highest among the certified ternary solar cells and one of the best certified single-junction cells<sup>32,34</sup>.

### A hierarchical morphology that governs device function

The encouraging device results persuaded us to investigate the structure details of ternary blends, which was accomplished by using grazing incidence wide-angle X-ray scattering (GIWAXS), transmission electron microscopy (TEM) and resonant soft X-ray scattering (RSoXS). Figure 2a–c shows the GIWAXS diffraction patterns, line-cut profiles and crystallinity analysis. The BTR in thin film shows quite strong structure order, with (100) diffraction at  $0.33 \text{ \AA}^{-1}$  in plane ( $q_{xy}$ ) and strong  $\pi$ – $\pi$  stacking at  $1.69 \text{ \AA}^{-1}$  out of plane ( $q_z$ ). The NITI shows weak crystallinity, with an in-plane (100) peak at  $0.36 \text{ \AA}^{-1}$  and broad  $\pi$ – $\pi$  stacking in the out-of-plane direction at  $1.79 \text{ \AA}^{-1}$ . Thus, both materials prefer a face-on orientation<sup>35</sup>. The BTR:PC<sub>71</sub>BM blend displays BTR molecular order and PC<sub>71</sub>BM diffuse scattering ring. The BTR  $\pi$ – $\pi$  stacking coherence length is estimated to be 5.39 nm by the Scherrer equation<sup>35</sup>, which is quite large for OPV materials. The BTR:NITI blend shows a much weaker structure order, where both the (100) and  $\pi$ – $\pi$  stacking peak intensity and size show sharp reductions. Thus, the presence of the NITI could retard BTR crystallization, indicating good material mixing. Such a mixed morphology and reduced structure order lead to poor carrier transport and, thus, device FF. Ternary blends with different NFA compositions show similar diffraction features. The (100) and  $\pi$ – $\pi$  stacking peak sizes are quite similar across a broad range of loading ratios (Supplementary Table 6), indicating that the presence of PC<sub>71</sub>BM leads to similar material ordering states for BTR (Supplementary Fig. 4), which is quite different compared with the NFA binary mixture. Thus, PC<sub>71</sub>BM works not only as a

transporting material (with low light absorption) but also a phase mediator to control the morphology of BHJ thin films.

The phase images of BHJ thin films were studied via bright-field and high-angle annular dark-field (HAADF) TEM, which has shown the ability to distinguish PCBM aggregates<sup>36</sup>. The results are shown in Fig. 2d. As seen from the BTR:PC<sub>71</sub>BM blend, dark aggregates are seen in the bright-field image, while they appear to be bright in the dark-field image. Such a feature is typical of a PC<sub>71</sub>BM-rich region, which is characterized as an intertwined network with an inter-distance of approximately 100 nm. The BTR:NITI blend shows a much more refined morphology (tens of nanometres), which is hard to see in the bright-field image but is clear in the HAADF image. Such a refined image can be highly efficient in exciton splitting, but the intimate mixing of the two materials results in high recombination, which reduces the current. The ternary BHJ blends show an interesting phase separation at a multi-length scale. Sharp white PC<sub>71</sub>BM domains are seen in the HAADF TEM, which suggests good domain connectivity. The domain spacing enlarges when NFA loading is high, which agrees well with the material composition. The presence of PC<sub>71</sub>BM in ternary BHJ blends makes it difficult to resolve more detailed structures within PC<sub>71</sub>BM-poor domains (BTR:NITI-rich domains). However, a morphology similar to that in the BTR:NITI blended thin film is expected. Such a morphology in ternary blends is similar to the city transportation system, where super highway arteries are interconnected by small roads to form a hierarchical network system. The detailed composition variation changes the ratio of super highways to small roads, which results in maximum transport efficiency (Supplementary Fig. 5). A power spectral density analysis was applied to HAADF TEM, but the low resolution led to poor statistical information on size (Supplementary Fig. 6). More detailed statistics on phase-separation size were studied via RSoXS by using a high-flux synchrotron X-ray and enhanced carbon k-edge contrast (284.2 eV)<sup>37</sup>. As seen from Fig. 2e, the BTR:PC<sub>71</sub>BM blend shows a sharp scattering peak at  $0.0088 \text{ \AA}^{-1}$ , which corresponds to a distance of 71.4 nm. The BTR:NITI blend shows a weak scattering profile in the high scattering vector ( $q$ ) region due to low material contrast. When NITI loading increases, the RSoXS profiles become broadened and shift towards a smaller  $q$  region (below  $0.01 \text{ \AA}^{-1}$ ), indicating

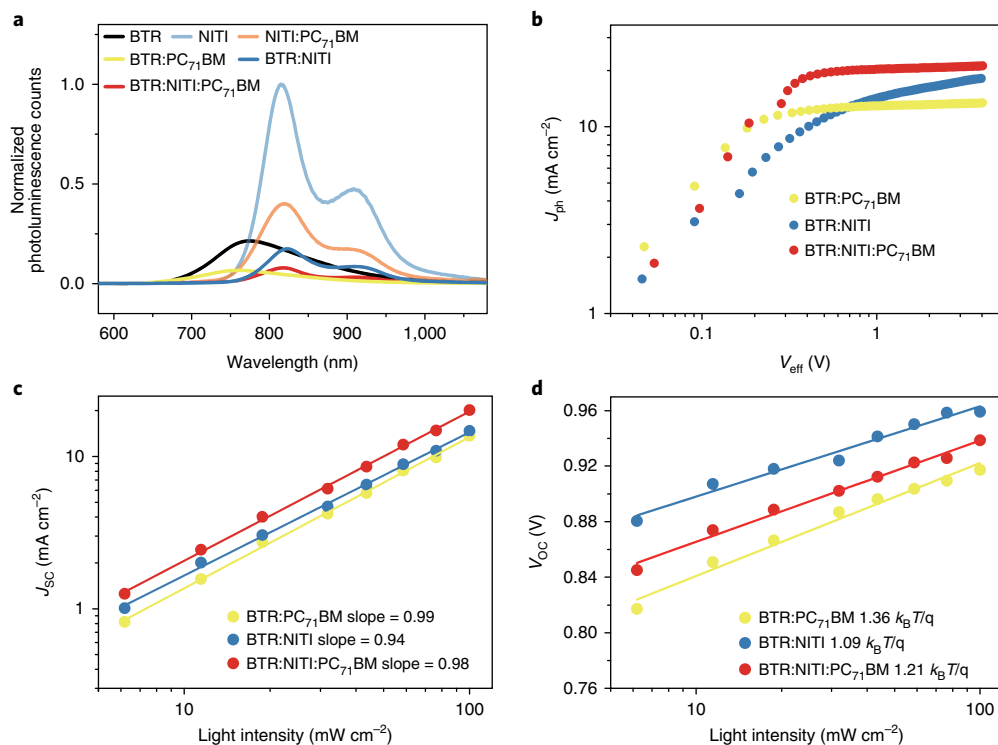


**Fig. 3 | Charge generation, extraction and recombination.** **a**, Photoluminescence spectra of the pristine donor, NFA and blended films. The intensities are corrected by their absorptions at the excitation wavelength (532 nm). **b**, Characteristics of the photocurrent density versus effective voltage ( $J_{ph} - V_{eff}$ ). **c**, Measurement of  $J_{sc}$  versus light intensity. **d**,  $V_{oc}$  versus light intensity for binary and ternary devices.

the irregular arrangement of super highways and increased inter-highway distance by swelling PC<sub>71</sub>BM domains, which agrees well with the TEM characterizations. The PC<sub>71</sub>BM framework and the in-between domains decorated with BTR crystallization-induced phase separation formulate the hierarchical structure in the ternary BHJ blends. Weak scattering anisotropy is seen in the ternary blends, with an increase in intensity in the vertical direction under the resonant scattering of polarized soft X-rays (Supplementary Fig. 7). Such a feature indicates that the PCBM:(BTR:NITI) domain interface has an orientation preference, where a slightly preferred face-on molecular orientation exists with respect to the PC<sub>71</sub>BM interface<sup>38</sup>. Such a feature is in favour of charge hopping and facilitates carrier transport. The current ternary blends are processed via spin-coating, followed by THF SVA, as such a treatment is crucial during morphology optimization and performance enhancement (Supplementary Table 1). The difference in material interactions, as estimated by the measured surface tension (Supplementary Fig. 8), shows that PC<sub>71</sub>BM has a much larger value than the BTR and NITI, which leads to large-scale phase separation via SVA<sup>39</sup>. The high-crystallinity BTR donor is expected to crystallize when the BHJ thin film is vitrified via THF vapours. The crystal growth of the BTR would expel the NITI molecules externally, which would jam at the PC<sub>71</sub>BM network framework interface to form a kinetically trapped structure with a smaller size phase separation and a preferred face-on orientation towards the PCBM. Such a morphology can be beneficial as transporting channels and exciton splitting sites manifest due to the hierarchical structure. The jamming of refined phase separation at multiple boundaries can also be of interest, as it can lock the system and enhance device stability; therefore, we checked the device storage stability (Supplementary Fig. 9). The PCE of the BTR:PC<sub>71</sub>BM device drops quickly to approximately 50% in approximately 500 h. However, the BTR:NITI:PC<sub>71</sub>BM ternary blend has a high PC<sub>71</sub>BM content, which shows stability better than that of the BTR:PC<sub>71</sub>BM device; we attribute these results to the benefits of the

hierarchical morphology and interfacial ordering of the NITI at the PC<sub>71</sub>BM domain surfaces.

The hierarchical morphology in the ternary blends helps to pin device parameters under optimized conditions for the corresponding binary blends, resulting in a  $V_{oc}$  similar to that in the BTR:NITI blend and large improvements in  $J_{sc}$  and FF. Such a morphology can be of general interest in OPV research. We extended this research to other material systems (with the results shown in Supplementary Figs. 10–12 and Supplementary Table 7) and realized several gauging parameters that lead to hierarchical morphology. There should be large-scale demixing between fullerene and other molecules and relatively good mixing between non-fullerene donor and acceptor materials, which could then phase separate via material crystallization. The inability to form refined phase separation in non-fullerene blends or good mixing between PC<sub>71</sub>BM and non-fullerene contents leads to a morphology without a defined hierarchy and, thus, no overall device parameter improvement. The molecular frameworks of donor and non-fullerene acceptor materials and side chains have significant impacts on morphological control (Supplementary Fig. 12). Preliminary in situ grazing incidence small-angle X-ray scattering (GISAXS) and GIWAXS printing experiments were carried out to investigate the morphology evolution process, which showed that large size phase separation occurs ahead of material crystallization (Supplementary Fig. 13)<sup>40</sup>, indicating that the formation of the PC<sub>71</sub>BM framework drives hierarchical morphology evolution.

### Optimized carrier dynamics to achieve high $J_{sc}$ and FF

The morphologies or interfaces between donors and acceptors determine charge generation and recombination in OPVs. To detect charge generation at the interface of thin films, the photoluminescence of ternary films is recorded. For comparison, reference films of pristine BTR, NITI and three binary blends are also measured and shown in Fig. 3a. The photoluminescence of pristine BTR has a broad emission with a peak at 770 nm. The spectrum of

NITI shows two peaks at 814 nm and 908 nm. As shown in Fig. 3a, approximately 30% photoluminescence in the BTR observed in BTR:PC<sub>71</sub>BM and complete BTR photoluminescence quenching in the BTR:NITI suggest large phase separation in the binary PC<sub>71</sub>BM and a fine mixture with a substantial number of exciton splitting sites in the binary NITI. In addition, only 17% photoluminescence in the NITI can be detected, indicating efficient hole transfer from the NITI to BTR. Interestingly, the photoluminescence of the ternary blend shows complete quenching of the pristine BTR and strong quenching (92%) of the pristine NITI, suggesting sufficient interfaces for efficient charge generation, which is consistent with the significantly enhanced  $J_{sc}$  of the corresponding devices. All of the above photoluminescence results indicate that the interface between the BTR and NITI dominates the process of charge generation in BTR:NITI:PC<sub>71</sub>BM. Furthermore, the photoluminescence of NITI:PC<sub>71</sub>BM shows 60% quenching of the pristine NITI, indicating a strong charge transfer from the NITI to PC<sub>71</sub>BM; however, such a feature does not lead to efficient NITI:PC<sub>71</sub>BM binary solar cells (Supplementary Table 8). Therefore, extra excitons from NITI can be further split by PC<sub>71</sub>BM. These photoluminescence experiments confirm the hierarchical morphology of the ternary blends.

Free carriers from exciton dissociation can be extracted and collected at electrodes or recombined to the ground state during a non-geminate process<sup>41,42</sup>. Charge generation, transport and extraction were studied by analysing the dependence of photocurrent density ( $J_{ph}$ ) on the effective voltage ( $V_{eff}$ ).  $J_{ph}$  is defined as  $J_{ph} = J_L - J_D$ , where  $J_L$  and  $J_D$  represent the current densities that are illuminated and in the dark, respectively.  $V_{eff}$  is defined as  $V_0 - V_a$ , where  $V_0$  represents the voltage when  $J_{ph}$  is 0 and  $V_a$  represents the applied voltage bias. As shown in Fig. 3b, the  $J_{ph}$  of both the fullerene-based binary and ternary devices increases to its saturation value ( $J_{sat}$ ) at a low  $V_{eff}$  of 2.0 V, with  $J_{sat}$  values of 14.22 and 20.16 mA cm<sup>-2</sup>, respectively. However, the NITI-based binary device does not show a saturation regime for  $J_{ph}$  (even at a  $V_{eff}$  of 4.0 V), indicating the high dependence of the electric field on charge carrier transport, which is consistent with low  $J_{sc}$  and FF values. In addition, the  $J_{ph}/J_{sat}$  ratio is also used to determine the overall efficiencies of exciton and charge collections. The fullerene-based binary and ternary devices show similar values of 97% and 86% under short-circuit and maximum output power conditions, respectively, suggesting that the PCBM presence is necessary in improving charge extraction and suppressing carrier recombination. The free carriers suffer from nongeminate recombination if they cannot be extracted and transported to the electrodes. Nongeminate recombination can be dominated by trap-assisted (monomolecular) or bimolecular mechanisms. The recombination mechanism was studied by measuring the dependencies of  $J_{sc}$  and  $V_{oc}$  on light intensity (Fig. 3c,d). The BTR:PC<sub>71</sub>BM and BTR:NITI:PC<sub>71</sub>BM blends show high figure-of-merit ( $\alpha$ ) values of 0.99 and 0.98, respectively, indicating extremely low bimolecular recombination. However, the BTR:NITI blend shows an  $\alpha$  of 0.94, which is the lowest value in this study. Thus, the NITI binary mixture suffers from recombination losses, which is a natural consequence of poor phase separation in blends. The relationship between  $V_{oc}$  and light intensity can be used to distinguish whether trap-assisted (slope of  $2k_B T/q$ , where  $k_B$  is Boltzmann's constant and  $T$  represents the absolute temperature) or bimolecular recombination ( $k_B T/q$ ) is the dominant mechanism. The BTR:NITI blend shows a small slope of  $1.09 k_B T/q$ , while the BTR:PC<sub>71</sub>BM blend shows a large slope of  $1.36 k_B T/q$ . Thus, the NITI binary mixture is dominated more by bimolecular recombination than the BTR:PC<sub>71</sub>BM blend, indicating inefficient carrier extraction and, hence, a low FF. A small amount of NITI in ternary blends can clearly reduce trap-assisted recombination in the BTR:PC<sub>71</sub>BM mixture (small slope of  $1.21 k_B T/q$ ), which indicates that the NITI can passivate energetic disorder at the phase boundary by routing the charge transfer from the BTR to NITI and then relaying to the PC<sub>71</sub>BM to form more favourable

transport pathways. Such a process can be efficient as the energy-level alignment is suitable to form a cascading charge transfer. Such material combination and morphology optimization yield overall improved  $J_{sc}$  and high FF values.

### Suppressing energy loss channel to improve $V_{oc}$

The high  $V_{oc}$  of the TOPVs ( $0.94 \pm 0.01$  V) motivates us to study the energy loss associated with the processes of exciton dissociation and carrier recombination. We use a model based on the Marcus theory that allows the energy of the charge-transfer state ( $E_{CT}$ ) to be determined from the part of the EQE spectrum with lower energy<sup>43</sup>.

$$EQE_{PV}(E) = \frac{f}{E\sqrt{4\pi\lambda k_B T}} \exp\left(\frac{-(E_{CT} + \lambda - E)^2}{4\lambda k_B T}\right) \quad (1)$$

where  $EQE_{PV}$  represents the photovoltaic EQE,  $f$  is proportional to the absorption strength of the charge-transfer state and the density of the donor/acceptor interfaces,  $\lambda$  represents the reorganized energy of the charge-transfer states and  $E$  represents the photon energy. Meanwhile, the total energy loss  $E_{loss}$  is equal to the summation of radiative recombination ( $\Delta E_1$ ), charge generation ( $\Delta E_2$ ) and the non-radiative recombination ( $\Delta E_3$ ) of energy losses, which can be determined according to the following equation<sup>19,44</sup>:

$$\begin{aligned} E_{loss} &= E_{gap} - qV_{oc} \\ &= \left[ -kT \ln\left(\frac{J_{sc} h^3 c^2}{2\pi f q (E_{CT} - \lambda)}\right) \right] \\ &\quad + (E_{gap} - E_{CT}) + [-kT \ln(EQE_{EL})] \\ &= \Delta E_1 + \Delta E_2 + \Delta E_3 \end{aligned} \quad (2)$$

where  $h$  is Planck's constant,  $c$  represents the speed of light and  $EQE_{EL}$  represents the electroluminescence EQE.

Specifically,  $\Delta E_2$  via photogenerated charge-transfer states is a dominating factor in dictating the  $V_{oc}$ , which is qualitatively investigated by using electroluminescence spectroscopy (Fig. 4a)<sup>19,45</sup>. A significant charge-transfer emission peaking at 990 nm is observed in the BTR:PC<sub>71</sub>BM blend, indicating a high-energy disorder at the interface of the BTR and PC<sub>71</sub>BM. However, the electroluminescence profiles of BTR:NITI and ternary blends are similar to those of the pristine NITI electroluminescence, which suggests that the charge-transfer states are similar to the lowest unoccupied molecular orbital of the NITI. More importantly, the absence of a charge-transfer emission at 990 nm in the ternary blend indicates negligible contact between the BTR and PC<sub>71</sub>BM; in other words, in the ternary blend, the NITI lies between the BTR and PC<sub>71</sub>BM, which blocks the energy loss channel of the BTR and PC<sub>71</sub>BM contacts. Furthermore, the highly sensitive Fourier transform photocurrent spectroscopy EQE (FTPS-EQE) was conducted to determine weak charge-transfer absorption (Fig. 4b).  $E_{CT}$  can be deduced by fitting the low energy region of the FTPS-EQE spectrum according to equation (1)<sup>46</sup>, and the results are summarized in Table 2. The  $E_{CT}$  values of the fullerene and non-fullerene BOPVs and TOPVs are 1.49, 1.43 and 1.42 eV, respectively. Surprisingly, the  $\Delta E_2$  of TOPVs (0.07 eV) is almost as small as that of the BTR:NITI device (0.06 eV) but far less than that of the BTR:PC<sub>71</sub>BM device (0.33 eV). The  $\Delta E_1$  values of the three kinds of devices are similar, which is unavoidable and less tunable for all kinds of solar cells<sup>19</sup>. However,  $\Delta E_3$  should be reduced with the specific materials optimization, as it is inversely and logarithmically dependent on  $EQE_{EL}$  (Fig. 4c). The  $\Delta E_3$  values of the BTR:NITI (0.26 eV) and ternary (0.30 eV) devices are similar and much lower than that of the BTR:PC<sub>71</sub>BM device (0.40 eV). Thus, the NITI could block the non-radiative decay channels in BTR:PC<sub>71</sub>BM to improve the  $V_{oc}$  of the device. In general, high  $E_{loss}$

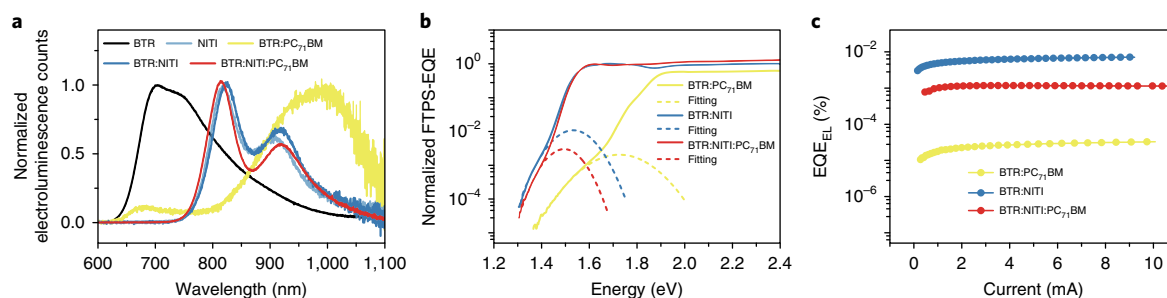


**Fig. 4 | Energy loss analysis.** **a**, Electroluminescence spectra of devices based on the pristine donor, NFA and blended films. **b**, Normalized FTPS-EQE of the blended devices. **c**, Normalized  $EQE_{EL}$  of the binary and ternary devices.

**Table 2 | Comparison between binary and ternary solar cells**

| BTR:NITI:PC <sub>71</sub> BM | $E_{gap}$ (eV) | $qV_{oc}$ (eV) | $E_{loss}$ (eV) | $f$ (eV <sup>2</sup> ) | $\lambda$ (eV) | $E_{CT}$ (eV) | $\Delta E_2$ (eV) | $\Delta E_1$ (eV) | $EQE_{EL}$ (%)       | $\Delta E_3$ (eV) |
|------------------------------|----------------|----------------|-----------------|------------------------|----------------|---------------|-------------------|-------------------|----------------------|-------------------|
| 1:0:1                        | 1.82           | 0.90           | 0.92            | $1.0 \times 10^{-3}$   | 0.24           | 1.49          | 0.33              | 0.19              | $1.8 \times 10^{-5}$ | 0.40              |
| 1:1:0                        | 1.49           | 0.95           | 0.54            | $3.0 \times 10^{-3}$   | 0.1            | 1.43          | 0.06              | 0.22              | $4.0 \times 10^{-3}$ | 0.26              |
| 1:0.4:1                      | 1.49           | 0.94           | 0.55            | $7.0 \times 10^{-4}$   | 0.08           | 1.42          | 0.07              | 0.18              | $8.2 \times 10^{-4}$ | 0.30              |

$$E_{loss} = E_{gap} - qV_{oc} = \Delta E_2 + \Delta E_1 + \Delta E_3$$

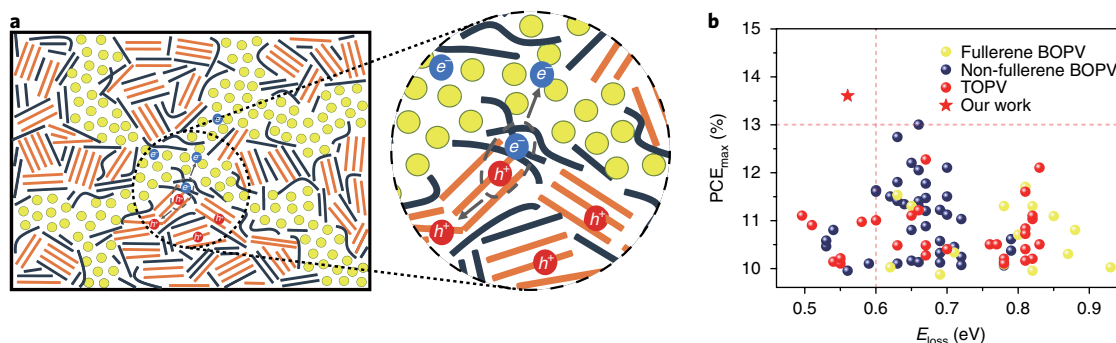


**Fig. 5 | Illustration of the morphology and comparison of  $PCE_{max}$  and  $E_{loss}$ .** **a**, Illustration of the hierarchical morphology in the ternary film and the dominant charge generation and transport processes. The green circles represent PC<sub>71</sub>BM, the navy rods represent NITI and the orange rods represent BTR. **b**, Plot of PCE versus  $E_{loss}$  for single-junction OPVs with efficiencies greater than 10%. Source references for the data points are provided in Supplementary Table 10.

in the BTR:PC<sub>71</sub>BM device (0.92 eV) and low  $E_{loss}$  in the BTR:NITI (0.54 eV) and TOPV (0.55 eV) devices are consistent with  $V_{oc}$  values in the corresponding photovoltaic devices. These exciting results show the importance of the new hierarchical morphology in simultaneously reducing energy losses and obtaining high  $J_{sc}$  and FF values, forming appropriate interfaces, suppressing unfavourable charge-transfer state and non-radiative recombination. Our work demonstrates that a similar  $V_{oc}$  (if not superior to non-fullerene BOPVs) can be obtained under proper ternary morphologies, while improved light absorption and transport provide further aid in driving the TOPV performance beyond that of any other binary blend.

## Conclusions

We designed interesting ternary blends using molecular donor (BTR), NFA (NITI) and fullerene acceptor (PC<sub>71</sub>BM) components that delivered a high device efficiency of  $13.20 \pm 0.25\%$  at a blend thickness of 300 nm (refs 47–49). We observed synergistic improvement in nearly all device parameters as well as charge transport and recombination, with a onefold PCE enhancement compared with the BTR:NITI BOPVs. Such an improvement was due to the hierarchical

morphology that was obtained from a balance between detailed phase separation and material crystallization, which showed that a subtle balance between the materials and interfaces was reached. A schematic of this morphology is shown in Fig. 5a. PC<sub>71</sub>BM in the ternary blend plays a critical role that phase separates with the NITI and BTR to form the morphological framework and provide efficient electron mobility. The BTR and NITI form a smaller size phase separation that fits into the PC<sub>71</sub>BM mesh network. We manipulate the thin-film morphology by using SVA, and BTR crystallization can push the NITI molecules out, which leads to material enrichment at the PC<sub>71</sub>BM boundary, with a slightly face-on orientation. Such a hierarchical morphology is particularly advantageous as the BTR:PC<sub>71</sub>BM charge-transfer state can be suppressed to reduce energy loss, and the carriers can be effectively transported via a cascading energetic channel. The NITI is key in improving the  $V_{oc}$  of the device. The PC<sub>71</sub>BM framework and good BTR crystallinity balance the carrier transport and reduce bimolecular recombination, which increases the  $J_{sc}$  and fill factor. We surveyed the most recent high-performance binary and ternary blends in terms of energy loss and the PCE (Fig. 5b and Supplementary Table 10). The current

work stands out. We attribute this success to the formation of the hierarchical morphology of the BHJ blend via proper material choice when identifying large-scale phase separation (PC<sub>71</sub>BM to the non-fullerene mixture) from the small-scale phase separation in the refined non-fullerene network. Such a strategy manifests the indispensability of fullerene and NFAs in OPVs, where new breakthroughs can be made in the near future.

## Methods

**Materials.** The BTR and PC<sub>71</sub>BM were purchased from 1-Material; all materials were used in the condition they were received, without further purification. The NITI was developed by our group<sup>25</sup>. The PNDIT-F3N was offered by the Fei Huang group.

**TEM.** TEM studies were conducted with a JEM-ARM200F microscope operated at 150 K. The samples for electron microscopy were prepared by dissolving the PEDOT:PSS layer using water and transferring the floating active layer to the TEM grids.

**GIWAXS.** The GIWAXS characterization of the thin films was performed at the Advanced Light Source on beamline 7.3.3 (Lawrence Berkeley National Laboratory). Thin-film samples were prepared under device conditions on the Si/PEDOT:PSS substrates. The scattering signal was recorded with the Pilatus 2M detector, with a pixel size of 0.172 mm by 0.172 mm. The samples were  $\approx 15$  mm long in the direction of the beam path, and the sample-to-detector distance was  $\approx 300$  mm from the sample centre (calibrated by the silver behenate standard). The incidence angle was 0.16°, and the beam energy was 10 keV when operating in top-off mode. Typically, a 30 s exposure time was used to collect the diffraction signals. All grazing incidence X-ray diffraction (GIWAX) experiments were done in a helium atmosphere. The data were processed and analysed using the Nika software package.

**RSoXS.** RSoXS was performed at beamline 11.0.1.2 (Advanced Light Source, Lawrence Berkeley National Laboratory). Thin-film samples were prepared under device conditions on the Si/PEDOT:PSS substrates. The BHJ thin films were then placed in water and transferred to a silicon nitride window. The scattering signals were collected in a vacuum using a Princeton Instrument-motion tracking enhancement technique (PI-MTE) charge-coupled device (CCD) camera.

**In situ structure measurement.** In situ GIWAXS/GISAXS experiments were performed using a customer-designed slot-die printer mounted on synchrotron beamline (Advanced Light Source beamline 7.3.3). The detailed experimental procedure and experimental videos can be obtained through ref.<sup>30</sup> Wafer coated with PEDOT:PSS was used as the printing substrate. The printing speed was  $\sim 80$  mm s<sup>-1</sup>, the die head to substrate distance was  $\sim 30$   $\mu$ m. An incidence angle of 0.16° was used in experiment. An AgB sample was used to calibrate the sample-to-detector distance. A Pilatus 1M or Pilatus 2M detector was used to record the scattering signals, and the data were analysed by the Nika software package. The scattering signal was recorded in burst mode with 0.2 s intervals. The wafer was first moved to printing position and aligned, and then moved to a start position that was away from beam path. The printing length is about 40 mm, and the solution injection triggered the in situ data recording. Experiments were repeated to ensure good time and space correlation.

**Photoluminescence measurement.** The pumping light source used to excite the samples was a green laser (532 nm), with a power of 10 mW. The photoluminescence spectra were recorded with an Andor spectrometer (Shamrock sr-303i-B), which was coupled with a Newton electron multiplying CCD detector.

**Electroluminescence measurement.** An external current/voltage source was employed to provide an external electric field to the pristine and blended solar cells. The electroluminescence emissions were recorded with an Andor spectrometer.

**FTPS-EQE measurement.** The FTPS-EQE was measured with a Vertex 70 from Bruker Optics, which was equipped with a quartz tungsten halogen lamp, quartz beam-splitter and external detector option. A low-noise current amplifier (SR570) was used to amplify the photocurrent produced under illumination of the solar cells, with light modulated by the Fourier transform infrared spectroscopy (FTIR). The output voltage of the current amplifier was fed back into the external detector port of the FTIR to use the FTIR software to collect the photocurrent spectra.

**EQE<sub>EL</sub> measurement.** The EQE<sub>EL</sub> was recorded with an in-house-built system comprising a Hamamatsu silicon photodiode 1010B, Keithley 2400 source meter (for supplying voltages and recording injected currents), and Keithley 485 picoammeter (for measuring the emitted light intensity).

**Device development and testing.** The devices were developed with a conventional structure of ITO/PEDOT:PSS/active layer/PNDIT-F3N/Al. The ITO-coated glass substrates were cleaned with sequential ultrasonication in a soap-deionized water mixture, deionized water, acetone and isopropanol. The washed substrates were further treated with oxygen plasma for 10 min to eliminate any remaining organic components. A thin layer (approximately 30 nm) of PEDOT:PSS (Clevios P VP 4083) was first spin-coated on the ITO substrates at 3,000 r.p.m. and baked at 150 °C for 5 min under ambient conditions. The substrates were then transferred into a nitrogen-filled glove box. Subsequently, the active layer was spin-coated on the PEDOT:PSS layer via spin-coating from a chloroform solution of BTR, NITI and PC<sub>71</sub>BM at various spin rates. The best PCE was achieved via spin-coating 25 mg BTR, 10 mg NITI and 25 mg PC<sub>71</sub>BM (1:0.4:1) in 1 ml chloroform at 1,500 r.p.m. The resultant film thickness was approximately 300 nm and obtained via a surface profilometer (Dektak XT, Bruker). Here, SVA with THF was used to optimize the blend morphology and promote device performance. SVA was conducted in a 60 mm glass Petri dish containing 200  $\mu$ l THF at various durations in a glove box. The optimal duration in this study was 60 s. Then, PNDIT-F3N (as the electron transport layer) was spin-coated on the active layer at 3,000 r.p.m. from the alcohol solution. In the final stage, aluminium (100 nm) was thermally evaporated onto the active layer as the top electrode. Shadow masks were used to define the device area (0.03262 cm<sup>2</sup>) of the devices. The current density–voltage (*J*–*V*) characteristics of the PV devices were measured under N<sub>2</sub> conditions using a Keithley 2400 source meter. An AAA grade solar simulator, with an air mass (AM) 1.5 global filter operated at 100 mW cm<sup>-2</sup>, was used to simulate the AM 1.5G solar irradiation. The illumination intensity was corrected by using a standard monocrystalline silicon reference cell, with a protective KG5 filter calibrated by the National Renewable Energy Laboratory. The *J*–*V* curves were measured along the forward scan direction from –0.2 to 1.5 V or the reverse scan direction from 1.5 to –0.2 V, yielding identical results. The scan speed and dwell times were fixed at 0.015 V s<sup>-1</sup> and 20 ms, respectively. The EQE was calculated using certified incident photon to current conversion efficiency equipment from Enlitech (Taiwan).

**SCLC mobility measurements.** SCLCs were tested in electron-only devices configured with the ITO/ZnO/active layer/Al and hole-only devices configured with the ITO/PEDOT:PSS/active layer/MoO<sub>3</sub>/Au. The mobilities were determined by fitting the dark-field current to the model of a single carrier SCLC current with field dependent mobility, which is described as

$$J = \frac{9\epsilon_0\epsilon_r\mu_0 V^2}{8L^3} \quad (3)$$

where *J* represents the current,  $\mu_0$  represents the zero-field mobility,  $\epsilon_0$  represents the permittivity of free space,  $\epsilon_r$  represents the relative permittivity of the material, *V* represents the effective voltage and *L* represents the thickness of the active layer. From the plot of *J*<sup>1/2</sup> versus *V*, the hole and electron mobilities can be deduced.

**Reporting Summary.** Further information on research design is available in the Nature Research Reporting Summary linked to this article.

## Data availability

The data that support the plots within this paper and other findings of this study are available from the corresponding authors upon reasonable request.

Received: 14 December 2017; Accepted: 2 August 2018;

Published online: 10 September 2018

## References

- Lu, L., Kelly, M. A., You, W. & Yu, L. Status and prospects for ternary organic photovoltaics. *Nat. Photon.* **9**, 491–500 (2015).
- Cheng, P. & Zhan, X. Versatile third components for efficient and stable organic solar cells. *Mater. Horiz.* **2**, 462–485 (2015).
- Ameri, T., Khoram, P., Min, J. & Brabec, C. J. Organic ternary solar cells: a review. *Adv. Mater.* **25**, 4245–4266 (2013).
- Gasparini, N. et al. Designing ternary blend bulk heterojunction solar cells with reduced carrier recombination and a fill factor of 77%. *Nat. Energy* **1**, 16118 (2016).
- Yang, Y. et al. High-performance multiple-donor bulk heterojunction solar cells. *Nat. Photon.* **9**, 190–198 (2015).
- Lu, L., Xu, T., Chen, W., Landry, E. S. & Yu, L. Ternary blend polymer solar cells with enhanced power conversion efficiency. *Nat. Photon.* **8**, 716–722 (2014).
- Huang, J.-S. et al. Polymer bulk heterojunction solar cells employing Förster resonance energy transfer. *Nat. Photon.* **7**, 479–485 (2013).
- Baran, D. et al. Reducing the efficiency–stability–cost gap of organic photovoltaics with highly efficient and stable small molecule acceptor ternary solar cells. *Nat. Mater.* **16**, 363–369 (2017).
- Kumari, T., Lee, S. M., Kang, S.-H., Chen, S. & Yang, C. Ternary solar cells with a mixed face-on and edge-on orientation enable an unprecedented efficiency of 12.1%. *Energy Environ. Sci.* **10**, 258–265 (2017).

10. Xu, X. et al. highly efficient ternary-blend polymer solar cells enabled by a nonfullerene acceptor and two polymer donors with a broad composition tolerance. *Adv. Mater.* **29**, 1704271 (2017).
11. Ryno, S. M., Ravva, M. K., Chen, X., Li, H. & Brédas, J.-L. Molecular understanding of fullerene–electron-donor interactions in organic solar cells. *Adv. Energy Mater.* **7**, 1601370 (2017).
12. Liu, T. & Troisi, A. What makes fullerene acceptors special as electron acceptors in organic solar cells and how to replace them. *Adv. Mater.* **25**, 1038–1041 (2013).
13. Lin, Y. & Zhan, X. Non-fullerene acceptors for organic photovoltaics: an emerging horizon. *Mater. Horiz.* **1**, 470–488 (2014).
14. Nielsen, C. B., Holliday, S., Chen, H. Y., Cryer, S. J. & McCulloch, I. Non-fullerene electron acceptors for use in organic solar cells. *Acc. Chem. Res.* **48**, 2803–2812 (2015).
15. Yan, H. et al. A high-mobility electron-transporting polymer for printed transistors. *Nature* **457**, 679–686 (2009).
16. Veldman, D., Meskers, S. C. J. & Janssen, R. A. J. The energy of charge-transfer states in electron donor–acceptor blends: insight into the energy losses in organic solar cells. *Adv. Funct. Mater.* **19**, 1939–1948 (2009).
17. Kawashima, K., Tamai, Y., Ohkita, H., Osaka, I. & Takimiya, K. High-efficiency polymer solar cells with small photon energy loss. *Nat. Commun.* **6**, 10085 (2015).
18. Gao, K. et al. Deep absorbing porphyrin small molecule for high-performance organic solar cells with very low energy losses. *J. Am. Chem. Soc.* **137**, 7282–7285 (2015).
19. Menke, S. M., Ran, N. A., Bazan, G. C. & Friend, R. H. Understanding energy loss in organic solar cells: toward a new efficiency regime. *Joule* **2**, 25–35 (2018).
20. Liu, J. et al. Fast charge separation in a non-fullerene organic solar cell with a small driving force. *Nat. Energy* **1**, 16089 (2016).
21. Collins, S. D., Ran, N. A., Heiber, M. C. & Nguyen, T.-Q. Small is powerful: recent progress in solution-processed small molecule solar cells. *Adv. Energy Mater.* **7**, 1602242 (2017).
22. Deng, D. et al. Fluorination-enabled optimal morphology leads to over 11% efficiency for inverted small-molecule organic solar cells. *Nat. Commun.* **7**, 13740 (2016).
23. Zhang, Q. et al. Small-molecule solar cells with efficiency over 9%. *Nat. Photon.* **9**, 35–41 (2015).
24. Sun, Y. et al. Solution-processed small-molecule solar cells with 6.7% efficiency. *Nat. Mater.* **11**, 44–48 (2011).
25. Xu, S. et al. An electron-rich 2-alkylthieno[3,4-*b*]thiophene building block with excellent electronic and morphological tunability for high-performance small-molecule solar cells. *J. Mater. Chem. A* **4**, 17354–17362 (2016).
26. Liu, F. et al. A thieno[3,4-*b*]thiophene-based non-fullerene electron acceptor for high-performance bulk-heterojunction organic solar cells. *J. Am. Chem. Soc.* **138**, 15523–15526 (2016).
27. Liu, F. et al. Efficient semitransparent solar cells with high NIR responsiveness enabled by a small-bandgap electron acceptor. *Adv. Mater.* **29**, 1606574 (2017).
28. Xu, S. J. et al. A twisted thieno[3,4-*b*]thiophene-based electron acceptor featuring a 14- $\pi$ -electron indenodindene core for high-performance organic Photovoltaics. *Adv. Mater.* **29**, 1704510 (2017).
29. Zhang, C. & Zhu, X. Thieno[3,4-*b*]thiophene-based novel small-molecule optoelectronic materials. *Acc. Chem. Res.* **50**, 1342–1350 (2017).
30. Liu, F. et al. Multifaceted regioregular oligo(thieno[3,4-*b*]thiophene)s enabled by tunable quinoidization and reduced energy band gap. *J. Am. Chem. Soc.* **137**, 10357–10366 (2015).
31. Sun, K. et al. A molecular nematic liquid crystalline material for high-performance organic photovoltaics. *Nat. Commun.* **6**, 6013 (2015).
32. Zhao, W. et al. Molecular optimization enables over 13% efficiency in organic solar cells. *J. Am. Chem. Soc.* **139**, 7148–7151 (2017).
33. Cui, C. et al. High-performance organic solar cells based on a small molecule with alkylthio-thienyl-conjugated side chains without extra treatments. *Adv. Mater.* **27**, 7469–7475 (2015).
34. Zhao, J. et al. Efficient organic solar cells processed from hydrocarbon solvents. *Nat. Energy* **1**, 15027 (2016).
35. Chen, W., Nikiforov, M. P. & Darling, S. B. Morphology characterization in organic and hybrid solar cells. *Energy Environ. Sci.* **5**, 8045–8074 (2012).
36. Gao, K. et al. Multi-length-scale morphologies driven by mixed additives in porphyrin-based organic photovoltaics. *Adv. Mater.* **28**, 4727–4733 (2016).
37. Chen, W. et al. Hierarchical nanomorphologies promote exciton dissociation in polymer/fullerene bulk heterojunction solar cells. *Nano. Lett.* **11**, 3707–3713 (2011).
38. Liu, F. et al. Relating chemical structure to device performance via morphology control in diketopyrrolopyrrole-based low band gap polymers. *J. Am. Chem. Soc.* **135**, 19248–19259 (2013).
39. Jiang, K. et al. Multiple cases of efficient nonfullerene ternary organic solar cells enabled by an effective morphology control method. *Adv. Energy Mater.* **8**, 1701370 (2018).
40. Pröller, S. et al. Following the morphology formation in situ in printed active layers for organic solar cells. *Adv. Energy Mater.* **5**, 1501580 (2015).
41. Proctor, C. M., Kuik, M. & Nguyen, T.-Q. Charge carrier recombination in organic solar cells. *Prog. Polym. Sci.* **38**, 1941–1960 (2013).
42. Cowan, S. R., Roy, A. & Heeger, A. J. Recombination in polymer-fullerene bulk heterojunction solar cells. *Phys. Rev. B* **82**, 245207 (2010).
43. Vandewal, K., Tvingstedt, K., Gadisa, A., Inganäs, O. & Manca, J. V. Relating the open-circuit voltage to interface molecular properties of donor: acceptor bulk heterojunction solar cells. *Phys. Rev. B* **81**, 125204 (2010).
44. Yao, J. et al. Quantifying losses in open-circuit voltage in solution-processable solar cells. *Phys. Rev. Applied* **4**, 014020 (2015).
45. Rao, A. et al. The role of spin in the kinetic control of recombination in organic photovoltaics. *Nature* **500**, 435–439 (2013).
46. Vandewal, K., Tvingstedt, K., Gadisa, A., Inganäs, O. & Manca, J. V. On the origin of the open-circuit voltage of polymer-fullerene solar cells. *Nat. Mater.* **8**, 904–909 (2009).
47. Duan, C., Huang, F. & Cao, Y. Solution processed thick film organic solar cells. *Polym. Chem.* **6**, 8081–8098 (2015).
48. Liu, X. et al. Low band gap conjugated polymers combining siloxane-terminated side chains and alkyl side chains: side-chain engineering achieving a large active layer processing window for PCE > 10% in polymer solar cells. *J. Mater. Chem. A* **5**, 17619–17631 (2017).
49. Gasparini, N. et al. High-performance ternary organic solar cells with thick active layer exceeding 11% efficiency. *Energy Environ. Sci.* **10**, 885–892 (2017).
50. Liu, F. et al. Printing fabrication of bulk heterojunction solar cells and in situ morphology characterization. *J. Vis. Exp.* **119**, e53710 (2017).

## Acknowledgements

We thank the National Basic Research Program of China (Program 973) (No. 2014CB643502), the National Key R&D Program of China (2017YFA0204700), the Strategic Priority Research Program of the Chinese Academy of Sciences (XDB12010200) and the National Natural Science Foundation of China (21572234, 21661132006) for their financial support. Portions of this research were carried out at beamlines 7.3.3 and 11.0.1.2 at the Advanced Light Source and Molecular Foundry at the Lawrence Berkeley National Laboratory, which was supported by the Department of Energy (DOE), Office of Science and Office of Basic Energy Sciences. Y.J. and F.Z. acknowledge financial support from the Swedish Research Council (VR621-2013-5561), the Swedish Government Strategic Research Area in Material Science on Functional Materials at Linköping University (Faculty Grant SFO-Mat-LIU No 200900971) and the China Scholarship Council (CSC201606920028).

## Author contributions

Z.Z. and Q.Y. fabricated and optimized the devices; S.X. synthesized the NITI; J.S., Y.Q. and F.L. performed the morphology characterization and analysis; Y.J. performed the photoluminescence, electroluminescence and FTPS-EQE experiments, which were supervised by F.Z.; and X.Z. conceived and directed the project. All authors discussed the results and substantially contributed to the preparation of the manuscript.

## Competing interests

The authors declare no competing interests.

## Additional information

**Supplementary information** is available for this paper at <https://doi.org/10.1038/s41560-018-0234-9>.

**Reprints and permissions information** is available at [www.nature.com/reprints](http://www.nature.com/reprints).

**Correspondence and requests for materials** should be addressed to F.L. or F.Z. or X.Z.

**Publisher's note:** Springer Nature remains neutral with regard to jurisdictional claims in published maps and institutional affiliations.

## Solar Cells Reporting Summary

Nature Research wishes to improve the reproducibility of the work that we publish. This form is intended for publication with all accepted papers reporting the characterization of photovoltaic devices and provides structure for consistency and transparency in reporting. Some list items might not apply to an individual manuscript, but all fields must be completed for clarity.

For further information on Nature Research policies, including our [data availability policy](#), see [Authors & Referees](#).

### ► Experimental design

#### Please check: are the following details reported in the manuscript?

##### 1. Dimensions

- Area of the tested solar cells  Yes  No Section "Device fabrication and testing"
- Method used to determine the device area  Yes  No The area of our device area was determined and certified at National Institute of Metrology, China (NIM). However, we do not have the detailed information for the method.

##### 2. Current-voltage characterization

- Current density-voltage (J-V) plots in both forward and backward direction  Yes  No The current-voltage (J-V) plots in forward is supplied in Figure 1d. Both forward and backward scans were conducted, which yielded identical results.
- Voltage scan conditions  Yes  No Section "Device fabrication and testing"  
*For instance: scan direction, speed, dwell times*
- Test environment  Yes  No Our devices were characterized at room temperature (ca. 25 Celsius degree) in glove box. And see Supplementary Figure 20.  
*For instance: characterization temperature, in air or in glove box*
- Protocol for preconditioning of the device before its characterization  Yes  No No preconditioning protocol.
- Stability of the J-V characteristic  Yes  No No hysteresis or other unusual behaviour was observed during the characterization of the solar cells. In general, organic solar cells do not have hysteresis problems.  
*Verified with time evolution of the maximum power point or with the photocurrent at maximum power point; see ref. 7 for details.*

##### 3. Hysteresis or any other unusual behaviour

- Description of the unusual behaviour observed during the characterization  Yes  No No hysteresis or other unusual behaviour was observed during the characterization of the solar cells. In general, organic solar cells do not have hysteresis problems.
- Related experimental data  Yes  No No hysteresis or other unusual behaviour was observed during the characterization of the solar cells.

##### 4. Efficiency

- External quantum efficiency (EQE) or incident photons to current efficiency (IPCE)  Yes  No Figure 1f & Supplementary Figure 2
- A comparison between the integrated response under the standard reference spectrum and the response measure under the simulator  Yes  No Figure 1f
- For tandem solar cells, the bias illumination and bias voltage used for each subcell  Yes  No Our devices were only fabricated for single solar cells.

##### 5. Calibration

- Light source and reference cell or sensor used for the characterization  Yes  No Section "Device fabrication and testing"
- Confirmation that the reference cell was calibrated and certified  Yes  No Section "Device fabrication and testing"

|   |  |  |
|---|--|--|
| Calculation of spectral mismatch between the reference cell and the devices under test  | <input type="checkbox"/> Yes<br><input checked="" type="checkbox"/> No | The spectral mismatch factor was determined at National Institute of Metrology, China (NIM). We do not have the detailed information for the method. |
| <b>6. Mask/aperture</b>   |  |  |
| Size of the mask/aperture used during testing   | <input type="checkbox"/> Yes<br><input checked="" type="checkbox"/> No | We did not use a mask during testing.  |
| Variation of the measured short-circuit current density with the mask/aperture area   | <input type="checkbox"/> Yes<br><input checked="" type="checkbox"/> No | We did not use a mask during testing.  |
| <b>7. Performance certification</b>   |  |  |
| Identity of the independent certification laboratory that confirmed the photovoltaic performance  | <input checked="" type="checkbox"/> Yes<br><input type="checkbox"/> No | Section "Performance enhancement in ternary solar cells" & Supplementary Figure 20   |
| A copy of any certificate(s)<br><i>Provide in Supplementary Information</i>   | <input checked="" type="checkbox"/> Yes<br><input type="checkbox"/> No | Supplementary Figure 20  |
| <b>8. Statistics</b>  |  |  |
| Number of solar cells tested  | <input checked="" type="checkbox"/> Yes<br><input type="checkbox"/> No | Caption "Figure 1d" & Table 1  |
| Statistical analysis of the device performance  | <input checked="" type="checkbox"/> Yes<br><input type="checkbox"/> No | Section "Performance enhancement in ternary solar cells" & Caption "Figure 1d" & Table 1   |
| <b>9. Long-term stability analysis</b>  |  |  |
| Type of analysis, bias conditions and environmental conditions<br><i>For instance: illumination type, temperature, atmosphere humidity, encapsulation method, preconditioning temperature</i> | <input checked="" type="checkbox"/> Yes<br><input type="checkbox"/> No | Section "A" & Supplementary Figure 9   |